

Optical characteristics of p-type GaAs-based semiconductors towards applications in photoemission infrared detectors

Y. F. Lao, A. G. U. Perera, H. L. Wang, J. H. Zhao, Y. J. Jin, and D. H. Zhang

Citation: *Journal of Applied Physics* **119**, 105304 (2016); doi: 10.1063/1.4943591

View online: <http://dx.doi.org/10.1063/1.4943591>

View Table of Contents: <http://scitation.aip.org/content/aip/journal/jap/119/10?ver=pdfcov>

Published by the [AIP Publishing](#)

Articles you may be interested in

[InGaAs/InAsSb strained layer superlattices for mid-wave infrared detectors](#)

Appl. Phys. Lett. **108**, 022106 (2016); 10.1063/1.4939904

[Modelling of current-voltage characteristics of infrared photo-detectors based on type – II InAs/GaSb super-lattice diodes with unipolar blocking layers](#)

AIP Advances **5**, 097132 (2015); 10.1063/1.4930978

[Growth of InGaAsP based asymmetric quantum well infrared photodetector using metalorganic vapor phase epitaxy](#)

J. Appl. Phys. **96**, 6799 (2004); 10.1063/1.1810203

[Demonstration of a 256×256 middle-wavelength infrared focal plane array based on InGaAs/InGaP quantum dot infrared photodetectors](#)

Appl. Phys. Lett. **84**, 2232 (2004); 10.1063/1.1688000

[Short wavelength \(1–4 \$\mu\$ m \) infrared detectors using intersubband transitions in GaAs-based quantum wells](#)

J. Appl. Phys. **83**, 6178 (1998); 10.1063/1.367488

A promotional banner for AIP Applied Physics Reviews. The background is a dark blue gradient with a bright light source on the right, creating a lens flare effect. On the left, there is a small image of a book cover for 'AIP Applied Physics Reviews' featuring a diagram of a layered structure. The main text 'NEW Special Topic Sections' is in large, white, bold font. Below it, 'NOW ONLINE' is in yellow, followed by 'Lithium Niobate Properties and Applications: Reviews of Emerging Trends' in white. The AIP Applied Physics Reviews logo is in the bottom right corner.

NEW Special Topic Sections

NOW ONLINE
Lithium Niobate Properties and Applications:
Reviews of Emerging Trends

AIP Applied Physics
Reviews

Optical characteristics of *p*-type GaAs-based semiconductors towards applications in photoemission infrared detectors

Y. F. Lao,¹ A. G. U. Perera,^{1,2,a)} H. L. Wang,³ J. H. Zhao,³ Y. J. Jin,⁴ and D. H. Zhang⁴

¹Department of Physics and Astronomy, Georgia State University, Atlanta, Georgia 30303, USA

²Center for Nano-Optics (CeNO), Georgia State University, Atlanta, Georgia 30303, USA

³State Key Laboratory of Superlattices and Microstructures, Institute of Semiconductors, Chinese Academy of Sciences, P.O. Box 912, Beijing 100083, China

⁴School of Electrical and Electronic Engineering, Nanyang Technological University, Singapore 639798, Singapore

(Received 21 October 2015; accepted 26 February 2016; published online 14 March 2016)

Free-carrier effects in a *p*-type semiconductor including the intra-valence-band and inter-valence-band optical transitions are primarily responsible for its optical characteristics in infrared. Attention has been paid to the inter-valence-band transitions for the development of internal photoemission (IPE) mid-wave infrared (MWIR) photodetectors. The hole transition from the heavy-hole (HH) band to the spin-orbit split-off (SO) band has demonstrated potential applications for 3–5 μm detection without the need of cooling. However, the forbidden SO-HH transition at the Γ point (corresponding to a transition energy Δ_0 , which is the split-off gap between the HH and SO bands) creates a sharp drop around 3.6 μm in the spectral response of *p*-type GaAs/AlGaAs detectors. Here, we report a study on the optical characteristics of *p*-type GaAs-based semiconductors, including compressively strained InGaAs and GaAsSb, and a dilute magnetic semiconductor, GaMnAs. A model-independent fitting algorithm was used to derive the dielectric function from experimental reflection and transmission spectra. Results show that distinct absorption dip at Δ_0 is observable in *p*-type InGaAs and GaAsSb, while GaMnAs displays enhanced absorption without degradation around Δ_0 . This implies the promise of using GaMnAs to develop MWIR IPE detectors. Discussions on the optical characteristics correlating with the valence-band structure and free-hole effects are presented.

© 2016 AIP Publishing LLC. [<http://dx.doi.org/10.1063/1.4943591>]

I. INTRODUCTION

In recent years, *p*-type optical transitions involving the valence bands (VBs)¹ have been shown to have potential applications in unipolar heterojunction photodetectors based on an internal photoemission (IPE) mechanism.^{2–7} The advantages of photodetection based on holes as reported initially in *p*-type quantum well infrared photodetectors (QWIPs)^{8–12} are due to the larger effective mass of the hole that leads to a lower dark current, and the strong mixing between the light and heavy hole that enables detection with the normal incidence illumination geometry.⁸ In comparison with *p*-type quantum well based detectors, the use of unipolar (*p*-type doped) heterojunctions without quantum confinement for holes provides broad-band spectral response, which can be easily tailored through barrier height control.⁶ This allows easy integration of photodetectors without much efforts in growing complicated quantum structures. Possible applications include integrated optoelectronic devices, where a doping region can be readily obtained via ion implantation. In addition, hole relaxation involving with the VBs displays a unique dynamics in which a longer lifetime of holes was observed.^{13,14} This characteristics has contributed to a hot-carrier detection concept being developed that allows wavelength-extended response beyond the standard limit set by the spectral rule $\lambda_c = hc/\Delta$,¹⁵ where λ_c is the maximum

wavelength limit and Δ is the characteristic energy of the optical transition during operation. The demonstration was carried out using *p*-type heterojunction structures.^{16,17} Expected applications include the photoconductive and photovoltaic devices with wavelength-extended capabilities and spectral tunability by varying the degree of the hot-carrier injection.

The heterojunction photodetectors operate based on the IPE process. The original development of IPE detectors can be traced back to the use of silicide Schottky diodes and demonstrated silicon-based infrared focal plane array.¹⁸ The typical IPE processes include (1) photoexcitation of carriers in the absorber (referred to as emitter), (2) the movement of photoexcited carriers towards the emitter-barrier interface, and (3) emission of photoexcited carriers at the interface over the potential barrier.

The optical characteristics of the emitter are of paramount importance to develop IPE detectors. By comparing with the *n*-type semiconductor being used as the emitter, the *p*-type semiconductor absorbs extra photons owing to optical transitions among three VBs, i.e., the light-hole (LH), heavy-hole (HH), and spin-orbit split-off (SO) bands, contributing to an absorption band spanning primarily from 1 to 10 μm for *p*-type GaAs.¹ The IVB absorption is featured by the singularities in the joint density of states (JDOS), i.e., Δ_0 and Δ_1 , with the corresponding energies of 0.339 eV (Ref. 19) and 0.224 eV (Ref. 20), respectively. The split-off gap (Δ_0)

^{a)}uperera@gsu.edu

results from the spin-orbit coupling and is thus subject to change in terms of the size of the atom. Adding additional elements into the GaAs lattice, e.g., In or Sb, will allow tuning the singularities and thus the IVB absorption.²¹

In this paper, we extend our studies on the optical characteristics of *p*-type GaAs as reported previously¹ to InGaAs, GaAsSb, and GaMnAs, all of which are grown on the GaAs substrate. InGaAs and GaAsSb are compressively strained on the GaAs substrate; GaMnAs has a slightly larger lattice constant²² than that of GaAs and is thus subject to compressive strain as well. As a supplement to the approach described in Ref. 1 based on the model dielectric function (DF), the present study employs a comprehensive DF consisting of many oscillator-like functions, by which particular modeling of individual optical transitions is no longer needed. This approach is convenient as far as different materials or structures are concerned. This paper addresses (1) the IVB absorption of GaAs-based semiconductors and its dependence on the VBs and (2) the candidacy of a dilute magnetic semiconductor (DMS)—GaMnAs for the development of IPE detectors.

The spectral response of the IPE detector is primarily determined by the absorbing properties of the emitter, which is, in turn, determined by the electronic structure of the VBs, as well as the concentration of holes. Utilizing semiconductor heterojunctions for the IPE detectors is subject to limitations, including (1) lower absorption coefficient of doped semiconductors compared to that of the metal which was initially used as the emitter in Schottky barrier detectors and²³ (2) the optical characteristics related to the electronic structure, for example, a response dip around 3.6 μm in *p*-type GaAs/AlGaAs detectors, which is undesired for the 3–5 μm detectors.

As a prototypical III-V DMS, GaMnAs is a *p*-type material and contains free holes; in particular, the hole concentration is much higher (e.g., 10^{21} cm^{-3})²⁴ than regular *p*-type semiconductors doped with non-magnetic dopant such as Be (up to 10^{19} cm^{-3}) or Carbon (up to 10^{20} cm^{-3}). It is thus possible to have an even higher absorption over *p*-type GaAs by using GaMnAs. Furthermore, with the increase of the hole concentration and the shift of the Fermi level downward deep into the VBs, as well as the increase of the plasma frequency,¹ the absorption peak shifts and becomes broadened due to enhanced carrier scatterings.²⁵ The consequence could be the removal of the absorption dip at Δ_0 . Diminishing the absorption dip at Δ_0 will be advantageous to fully cover the 3–5 μm range of detection.

To determine the optical characteristics of semiconductors, DF modeling has been carried out.¹ The procedure includes optimizing the fitting parameters of the DF model so that the calculated reflection, transmission, and absorption agree with the experimental data. DF is a complex function that describes a number of optical processes, including the optical transitions involving different energy bands, and the phonon-photon interactions. Through DF, optical constants such as optical absorption, conductivity, and the index of refraction can be readily obtained. The computation of DF from optical transitions can be carried out by using a textbook formula²⁶

$$\varepsilon_2(E) = \frac{\hbar^2 e^2}{8\pi^2 \varepsilon_0 m_0^2 E^2} \sum_{ij} \int_{\text{BZ}} d\mathbf{k} \overline{|\hat{\mathbf{e}} \cdot \mathbf{p}_{ij}|^2} \delta \times [E_j(\mathbf{k}) - E_i(\mathbf{k}) - E](f_i - f_j), \quad (1)$$

where $\varepsilon_2(E)$ is the imaginary component of the DF, E is the photon energy, m_0 is the mass of a free electron, \mathbf{k} is the wave vector at which transitions take place, $\hat{\mathbf{e}}$ is a unit vector in the direction of the optical electric field, \mathbf{p}_{ij} is the momentum matrix element, $E_{i(j)}(\mathbf{k})$ is the energy of states for band $i(j)$, and $f_{i(j)}$ is the Fermi-Dirac (FD) distribution function representing occupation probability. The other symbols have their usual meaning. The δ function denotes the energy conservation. A factor of 2 due to two-fold spin degeneracy is not explicitly included. Therefore, i and j represent the indices of energy states with different spin states distinguished for one band. Equation (1) can be simplified to analytical functions by making approximations that, in the vicinity of singularities of the JDOS (the corresponding wave vectors are the critical points (CPs)), the JDOS is expanded into polynomial \mathbf{k} terms.^{27,28} This is applicable to the (valence) band-to-(conduction) band (BB) transitions, as well as the IVB transitions. The details of deducing analytical functions for IVB DF by taking the parabolic-band approximation can be found in Ref. 1.

In the presence of free holes, in addition to the IVB transitions, intra-band indirect transitions can be described by the classic Drude theory²⁹ which has been employed for doped materials in previous works.^{30–34} The IVB transitions are primarily responsible for the absorption from the short-wave detector⁵ (1–4 μm) and the long-wave detector⁶ (4–14 μm). As the optical transitions typically take place in the vicinity of the Γ point, the analytical form of the IVB DF is valid for the most of the cases. However, the strain effect, which is present in samples InGaAs, GaAsSb, and GaMnAs (on GaAs) under study, influences the band profile,³⁵ and therefore, the parabolic-band approximation is no longer valid.

II. THEORETICAL MODEL

The real (ε_1) and imaginary (ε_2) components of the DF must satisfy the Kramers-Kronig (K-K) relation, i.e.,

$$\varepsilon_1(\omega) = 1 + \frac{2}{\pi} \mathcal{P} \int_0^{+\infty} \frac{\omega' \varepsilon_2(\omega')}{\omega'^2 - \omega^2} d\omega', \quad (2)$$

where \mathcal{P} denotes the principal value of the integral. To obtain a universal DF independent of particular optical processes and materials or structures, multiple oscillator-like mathematical functions are used to construct the DF. The idea is that the DF of individual optical process, such as the BB and IVB transitions, can be expanded into basic functions, for example, with the following form:

$$\varepsilon(\omega) = \varepsilon_\infty + \sum_{j=1}^N \frac{\omega_{p,j}^2}{\omega_{0,j}^2 - \omega^2 - i\omega\Gamma_j} + \sum_{k=2}^{M-1} A_k [\varepsilon_1^k(\omega) + i\varepsilon_2^k(\omega)], \quad (3)$$

where ε_∞ is the high-frequency dielectric constant; N and M are the number of functions, determined by the fitting. The

second and third terms (Eq. (3)) correspond to the Lorentz and localized functions, respectively.

An optical spectrum is usually a result of various optical processes associated with the material itself and other influences from, for example, the dopants or impurities. In most of the cases, only those that have the dominating effects are considered.¹ By using a comprehensive DF of Eq. (3), all of the features shown on the spectrum are able to be taken into account, and therefore, a “perfect” fitting can be achieved. The fitting will be dependent on the number of terms used in Eq. (3); this means that a great number of functions are needed to produce a “perfect” fitting. As such, this DF model is basically a mathematical manipulation and does not have the corresponding physical processes. Nevertheless, this approach is very useful and serves as the way of converting the experimental data (transmission and reflection) into a DF. Apparently, the advantage lies in the inclusion of all of possible optical processes such as the BB and IVB transitions, the transitions involving impurity levels or bands, and the doping-induced band tailing states, intra-band free-carrier (FC), and phonon absorption.

The coupling of the electromagnetic wave to the transverse optical (TO) phonon modes in a polar crystal can be modeled as harmonic oscillators,¹ which are handled by the second term of Eq. (3), the Lorentz oscillators, in which $\omega_{p,j}$, $\omega_{0,j}$, and Γ_j are the amplitude, frequency, and damping constant, respectively. For $\omega_{0,j} \neq 0$, it exemplifies the type of oscillators accounting for the contributions of the phonons to the DF; when $\omega_{0,j} = 0$, it can be interpreted to be the FC effect in terms of the Drude theory, with $\omega_{p,j}$ the plasma frequency.²⁹ Therefore, the second term of Eq. (3) accounts for the important and dominating features in the far infrared (FIR) region by the phonon and FC absorption. The Lorentz oscillators have the global effects on the entire spectral range and cannot replicate fine features. One of the approaches for this is to limit the number of Lorentz oscillators being used, as well as adding localized functions which are handled by the third term of Eq. (3), where A_k is the amplitude. Here, $\varepsilon_1^k(\omega)$ is obtained by carrying out the K-K transformation on $\varepsilon_2^k(\omega)$; $\varepsilon_2^k(\omega)$ consists of localized functions, as constructed with the following triangle function:³⁶

$$\varepsilon_2^k(\omega) = \begin{cases} \frac{\omega - \omega_{k-1}}{\omega_k - \omega_{k-1}}, & \omega_{k-1} < \omega \leq \omega_k \\ \frac{\omega_{k+1} - \omega}{\omega_{k+1} - \omega_k}, & \omega_k < \omega \leq \omega_{k+1}, \end{cases} \quad (4)$$

which is defined in the spectral region of $[\omega_{k-1}, \omega_{k+1}]$. It is apparent that the triangle function should be limited to a reasonably small range to mimic the experiments.

To fit the experimental spectra, all of the unknown parameters in Eq. (3) are taken as fitting parameters and determined by using the Levenberg-Marquardt method. The fitting accomplished in this study is divided into two steps: (1) determining the global Lorentz oscillators and then (2) refining the localized functions. Usually, it is necessary to include a great number of oscillators or localized terms (Eq. (4)) to achieve a “perfect” fitting, which means a great

deal of computation time is required. A better implementation is to repeat the fitting iteratively, i.e.,

$$\varepsilon_m(\omega) = \varepsilon_{m-1}(\omega) + \sum_{k'=2}^{M'-1} A_{k'} [\varepsilon_1^{k'}(\omega) + i \varepsilon_2^{k'}(\omega)], \quad (5)$$

where $\varepsilon_{m-1}(\omega)$ is obtained from the prior fitting, and $\varepsilon_m(\omega)$ is the new DF.

Using a large number of Lorentz oscillators should be avoided, in order to mitigate the global influence of the oscillators on the DF. In a typical fitting, two oscillators,¹ which correspond to the plasma effect and the coupling of electromagnetic waves to the TO phonon modes in a polar crystal,²⁹ can account for the dominant features in the far infrared region. For the mid-wave infrared (MWIR) regions, the SO-HH and LH-HH transitions dominate, each of which can be represented by one oscillator. As can be seen, the number of fitting parameters used in the localized functions mainly determines the computation time. In practice, they can be significantly reduced by putting ω_k on a mesh with a fixed pattern, with either equal³⁶ or unequal spacing. In consideration of the detailed features such as the multiple phonons in the far infrared region, the unequal spacing is efficient. We have applied a mesh with a pattern of logarithmical distribution.

The fittings include the complex index of refraction of each stratified layer derived from the DF, and then the calculation of the reflection and transmission for the sample, schematically shown in Fig. 1(a), consisting of a thin film on a substrate. The calculation is carried out based on an intensity-transfer-matrix method (ITMM). A TMM is used to take into account the coherence of the forward and backward traveling waves due to the interfacial reflection in the film. However, non-coherence should be considered to deal with the substrate, since its thickness is of the order of magnitude of $10^2 \mu\text{m}$.

The details of TMM are described below. Labeling a layer as j , with $j = 1$ denoting the topmost layer, and assuming that N is the total number of layers, we can write out the electric field of the light (transverse electric (TE) polarization)

$$\mathbf{E}^j = [A_j e^{ik_z^j(z-z_j)} + B_j e^{-ik_z^j(z-z_j)}] e^{ik_x^j x} \hat{\mathbf{e}}_y, \quad (6)$$

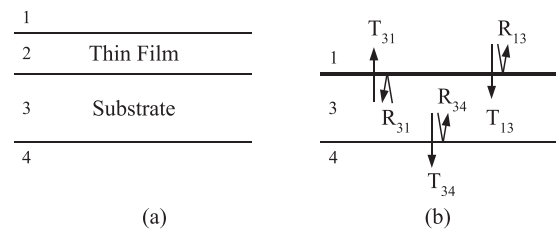


FIG. 1. (a) Schematic of the thin film sample, which consists of a thin film grown on a substrate. The thickness of the structure is in the order of magnitude of $10^2 \mu\text{m}$ (see Table I). (b) The equivalent structure of (a) to calculate the reflectivity and transmissivity of the entire structure, where light propagation inside the substrate is considered to be non-coherent. The interface between media 1 and 3 represents for the thin film. The reflectivity and transmissivity (i.e., R_{13} and T_{13} and R_{31} and T_{31}) at this interface are calculated by using TMM. R_{34} and T_{34} are calculated by using Fresnel equations.

where \hat{e}_y is a unit vector of the y-axis perpendicular to the incident plane. We assume that the growth direction is along the z-axis. $k_x^j(k_z^j)$ is the $x(z)$ component of the wave vector \mathbf{k}^j in the layer j . z_j is the coordinate of the interface (labeled as j) which is located between the layer j and $j + 1$. A_j and B_j are the amplitudes of the forward and backward waves, respectively. The magnetic field \mathbf{H}^j can be obtained from one of the Maxwell's equations, i.e., $\mathbf{H}^j = \nabla \times \mathbf{E}^j / i\omega\mu_j$ in which ω is the angular frequency and μ_j is the permeability of free space (μ_0). Taking the following boundary conditions:

$$E_y^{j-1}(z_{j-1}) = E_y^j(z_{j-1}) \text{ and } H_x^{j-1}(z_{j-1}) = H_x^j(z_{j-1}), \quad (7)$$

the transfer matrix is deduced as

$$M_{j-1,j} = \frac{1}{2} \begin{bmatrix} \left(1 + \frac{P_j}{P_{j-1}}\right) e^{-i\beta_j} & \left(1 - \frac{P_j}{P_{j-1}}\right) e^{i\beta_j} \\ \left(1 - \frac{P_j}{P_{j-1}}\right) e^{-i\beta_j} & \left(1 + \frac{P_j}{P_{j-1}}\right) e^{i\beta_j} \end{bmatrix}, \quad (8)$$

where $P_j = k_x^j / \omega\mu_j$ and $\beta_j = k_z^j d_j$ with $d_j = z_j - z_{j-1}$. d_j is the thickness of layer j . For $j = N + 1$ which corresponds to the outgoing medium, the transfer matrix is calculated by setting $d_{N+1} = 0$. $M_{j-1,j}$ connects the electric field of light in the two layers below and above interface j via the following relationship:

$$\begin{bmatrix} A_{j-1} \\ B_{j-1} \end{bmatrix} = M_{j-1,j} \begin{bmatrix} A_j \\ B_j \end{bmatrix}. \quad (9)$$

The formalism of the transfer matrix for transverse magnetic (TM) polarization can be obtained by applying the duality principle, i.e., $\mathbf{E} \rightarrow \mathbf{H}$, $\mathbf{H} \rightarrow -\mathbf{E}$, $\mu \rightarrow \varepsilon$ and $\varepsilon \rightarrow \mu$. This leads to the same expression as Eq. (8) except that P_j is now defined as $k_x^j / \omega\varepsilon_j$.

The total transfer matrix M is obtained by repeating Eq. (9), which turns out to be the multiplication of the matrix from layer 0 through layer $N + 1$ ($j=0$ denotes the incoming medium), i.e., $M = \prod_{j=1}^{N+1} M_{j-1,j}$. In terms of M , the reflectivity and transmissivity of the film can be calculated using

$$R_{13} = \left| \frac{M_{21}}{M_{11}} \right|^2 \quad \text{and} \quad T_{13} = \frac{\text{Re}(P_{N+1})}{\text{Re}(P_0)} \cdot \left| \frac{1}{M_{11}} \right|^2, \quad (10)$$

where the subscripts are explained in Fig. 1. To obtain the total reflectivity and transmissivity of the entire structure, the substrate has to be taken into account by using ITMM. This is done in terms of the structure shown in Fig. 1(b). A special (top) interface denotes the film (or multiple layers). The reflection and transmission (including R_{31} and T_{31}) can be readily obtained by applying TMM on the film. The problem is then converted into a one-layer structure, with the following non-coherent formula:

$$R_{14} = R_{13} + \frac{T_{13}R_{34}T_{31}e^{-2\alpha_3 d_3}}{1 - R_{34}R_{31}e^{-2\alpha_3 d_3}}, \quad T_{14} = \frac{T_{13}T_{34}e^{-2\alpha_3 d_3}}{1 - R_{34}R_{31}e^{-2\alpha_3 d_3}}, \quad (11)$$

where α_3 and d_3 are the absorption coefficient and thickness of the substrate. R_{34} and T_{34} are calculated by using Fresnel equations

$$R_{34} = \left| \frac{N_3 - N_4}{N_3 + N_4} \right|^2 \quad \text{and} \quad T_{34} = \text{Re} \left(\frac{N_4}{N_3} \right) \cdot \left| \frac{2N_3}{N_3 + N_4} \right|^2, \quad (12)$$

where N is the complex index of refraction of the corresponding layer shown in Fig. 1. The above formulation is deduced under the condition of the normal or near normal incidence.

III. EXPERIMENT

The samples used in this study include InGaAs, GaAsSb, and GaMnAs, consisting of a p -type layer grown on the double-side polished semi-insulating GaAs substrate. InGaAs and GaMnAs were grown by Molecular Beam Epitaxy (MBE), while GaAsSb was grown by Metal Organic Chemical Vapor Phase Deposition (MOCVD). The concentration of holes in samples InGaAs and GaAsSb can be regarded as being the same as the p -type doping concentration which is $5 \times 10^{18} \text{ cm}^{-3}$ (nominal value). Mn in GaMnAs can be donor (interstitial) or acceptor (substitutional Mn_{Ga}),³⁷ which causes the variation of the hole concentration to depend on the experimental conditions. Table I shows the structural parameters of these samples.

A Bruker Vertex 70 Fourier Transform InfraRed (FTIR) spectrometer was used to measure the reflection and transmission spectra from 150 cm^{-1} to 8000 cm^{-1} at room temperature (RT). The FTIR spectrometer is equipped with a Parker Balston Purge Gas Generator to provide a purified purge gas. For the spectral range between 150 and 450 cm^{-1} , a RT-DTGS FIR detector and a Si beamsplitter were used; for the range between 450 and 8000 cm^{-1} , a RT-DLaTGS detector along with a KBr beamsplitter was used. All spectra were acquired using a resolution of 4 cm^{-1} . The transmission and reflection were measured with the light at the normal incidence, and at 8° of the incidence angle, respectively.

IV. RESULTS AND DISCUSSION

The Van Hove singularities of JDOS have the crucial influence on the optical absorption. The singularities correspond to these wave vectors at which the two energy bands that the transition involves become parallel. Δ_0 is defined as the energy gap between the SO and HH bands at $k=0$ (Γ point), i.e., the split-off gap. Δ_1 is the energy gap between the LH and HH bands at large values of the wave vectors

TABLE I. The p -type GaAs-based semiconductor samples for optical studies.

Samples	Thickness of the film (μm)	Thickness of GaAs substrate (μm)
$\text{In}_{0.15}\text{Ga}_{0.85}\text{As}/\text{GaAs}$	0.10	350 ± 20
$\text{GaAs}_{0.955}\text{Sb}_{0.045}/\text{GaAs}$	0.19	650 ± 20
$\text{Ga}_{0.97}\text{Mn}_{0.03}\text{As}/\text{GaAs}$	0.10	350 ± 20
$\text{Ga}_{0.94}\text{Mn}_{0.06}\text{As}/\text{GaAs}$	0.10	350 ± 20

(along the Λ direction towards the L point), where LH and HH bands run in parallel. Although a strong saddle-point singularity is expected in the SO-LH transition, it has an insignificant effect on the absorption, because of the lower hole occupancy in the LH band in most of the cases. By increasing the number of holes in the LH band, this singularity should be observable in experiment. The characteristics of the IVB absorption can be understood in terms of Δ_0 and Δ_1 . Based on the previously reported DF model,¹ Fig. 2 plots (a) real (ε_1) and (b) imaginary (ε_2) component of DF, and (c) absorption coefficient for p -type GaAs at different doping concentration. The LH-HH transition primarily occurs below Δ_1 , while the SO-HH transition requires a higher photon energy than Δ_0 . With the increase of the doping concentration, the Fermi level moves downward and the LH-HH transitions take place at large values of the wave vectors (see, for example, Fig. 1(a) of Ref. 6). The absorption peak moves from around $8.5 \mu\text{m}$ at $p = 10^{17} \text{cm}^{-3}$ to $5.5 \mu\text{m}$ at $p = 10^{20} \text{cm}^{-3}$ which is nearly the equivalent wavelength of Δ_1 ($5.54 \mu\text{m}$) for GaAs.⁶

The value of Δ_0 is the onset of the SO-HH transition; its value can be derived from $d(\text{JDOS})/d\hbar\nu$.¹⁹ In consideration of $\text{JDOS} \sim \alpha$ (where α is the absorption coefficient), we plot $d\alpha/d\hbar\nu$ as shown in Fig. 2(d) for different doping concentration. It can be seen that $d\alpha/d\hbar\nu$ vanishes ($< 10^{19} \text{cm}^{-3}$) at about 0.34eV which is consistent with the value of 0.339eV determined by IPE spectroscopy.¹⁹ By increasing the doping concentration to be greater than 10^{19}cm^{-3} , the dominant SO-HH transitions take place at large values of the wave vectors, leading to the move of the $d\alpha/d\hbar\nu$ vanishing point to the higher energy. Therefore, the absorption behavior at very high doping concentration should not be used to predict Δ_0 .

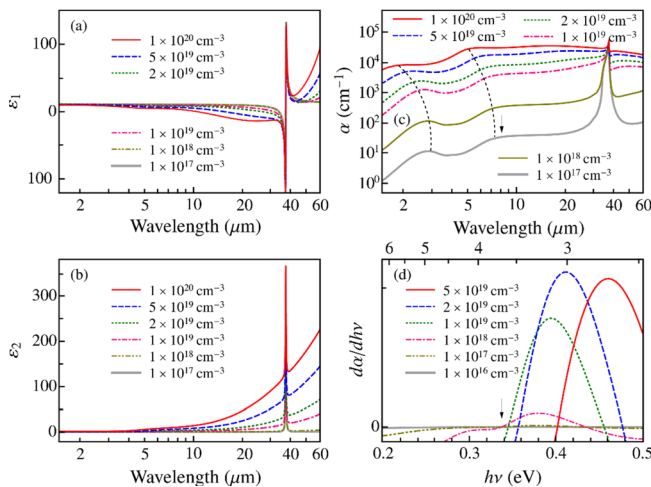


FIG. 2. The optical constants of p -type GaAs at different doping concentrations based on the model described in Ref. 1: (a) real (ε_1) and (b) imaginary (ε_2) component of the dielectric function, and (c) absorption coefficient (α), where the arrow shows the absorption peak for a doping concentration of $1 \times 10^{17} \text{cm}^{-3}$. The two dashed lines indicate the SO-HH and LH-HH transitions at different doping concentrations. (d) is the derivative of the absorption, which predicts (see details in the text) the split-off gap Δ_0 by $d\alpha/d\hbar\nu = 0$. The arrow shows the vanishing point of $d\alpha/d\hbar\nu$ for doping concentrations less than $1 \times 10^{19} \text{cm}^{-3}$; for higher doping concentrations, the vanishing point moves to higher energies.

The DF and absorption characteristics of p -type GaAs-based films in this study are determined using the method described in Sec. II. The DF model with fitting parameters should be applied only to one of the layers in the sample, and the DF of the rest of the materials should be known. This means that fitting to the spectra of the GaAs substrate should be carried out at the first place. And then, the obtained DF of GaAs is used to fit the film samples. Figure 3(a) shows the fittings to both reflection and transmission of the double-side polished semi-insulating GaAs substrate, from which the DF and absorption coefficient are obtained as shown in Figs. 3(b) and 3(c), respectively. The multiple peaks in the reststrahlen region belong to the features of the phonons. The dashed lines shown in the inset of Fig. 3(c) indicate the TO ($37.4 \mu\text{m}$)¹⁹ and the multiple phonons in terms of the Table XI of Ref. 38; they are in good agreement with the positions of the multiple peaks.

To fit the spectra of the film samples, ITMM is used to calculate the reflection and transmission by constructing a DF based on Eq. (3) for the film. The fitting results are shown in Figs. 4(a)–4(d) for $\text{In}_{0.15}\text{Ga}_{0.85}\text{As}$, $\text{GaAs}_{0.955}\text{Sb}_{0.045}$, $\text{Ga}_{0.97}\text{Mn}_{0.03}\text{As}$, and $\text{Ga}_{0.94}\text{Mn}_{0.06}\text{As}$, respectively. A good match between the fittings and experimental spectra is achieved, mainly because of those localized functions used in Eq. (3) that handle the fine features very well. However, it should be noted that the uncertainties or spectral noise from experiments will appear on the fitted spectral DF as well, which have to be discerned and excluded in terms of the

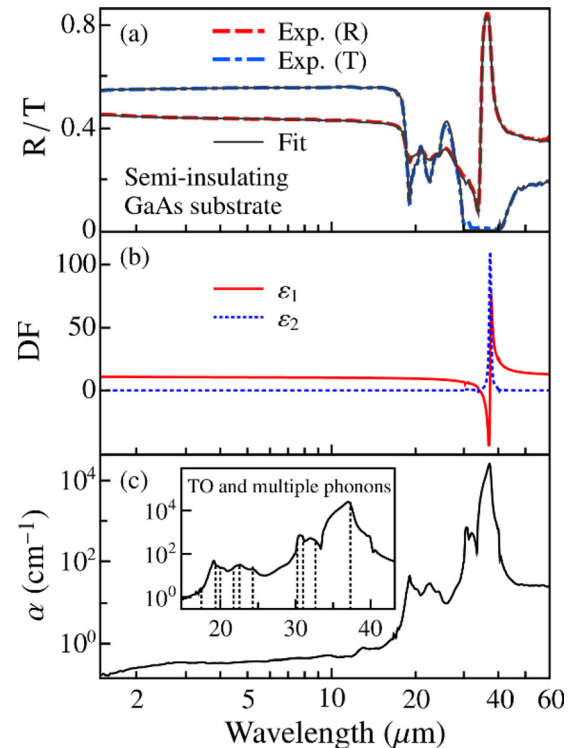


FIG. 3. (a) Experimental reflection and transmission spectra of double-side polished semi-insulating GaAs substrate. The fittings were carried out using the method described in Sec. II. (b) and (c) are the dielectric function (DF) and absorption coefficient (α) which are determined from the fittings. The reststrahlen region is shown in detail in the inset, where the vertical dashed lines indicate the TO ($37.4 \mu\text{m}$) (Ref. 19) and the multiple phonons in terms of the Table XI of Ref. 38.

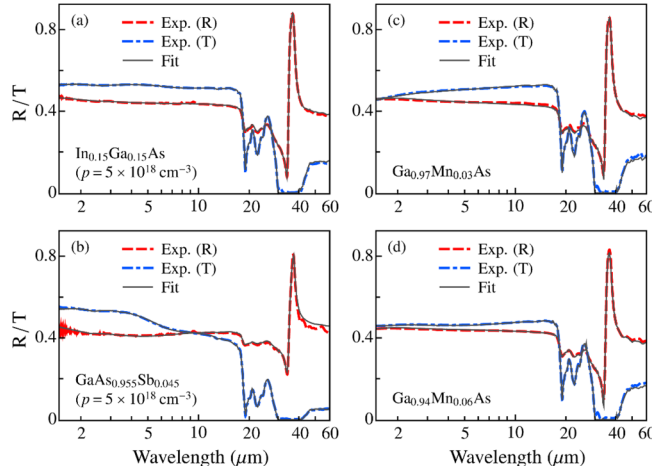


FIG. 4. Comparison of the experimental spectra (reflection and transmission) and the fittings (based on the method described in Sec. II) for (a) $\text{In}_{0.15}\text{Ga}_{0.85}\text{As}$, (b) $\text{GaAs}_{0.955}\text{Sb}_{0.045}$, (c) $\text{Ga}_{0.97}\text{Mn}_{0.03}\text{As}$, and (d) $\text{Ga}_{0.94}\text{Mn}_{0.06}\text{As}$. A good match between the fittings and experimental spectra is achieved, mainly because of the use of the localized functions in Eq. (3).

actual optical processes taking place in the sample such as the SO-HH transition, free-carrier absorption, and so on.

The DF spectra of p -type $\text{In}_{0.15}\text{Ga}_{0.85}\text{As}$ and $\text{GaAs}_{0.955}\text{Sb}_{0.045}$ are shown in Fig. 5, with the insets showing the phonon region. Fig. 6 plots the absorption coefficient derived from DF. A comparison among the non-magnetic p -type samples including InGaAs, GaAsSb, and GaAs indicates the shifting of the absorption peak (between 1 and 5 μm) associated with the SO-HH transition. The energy value of Δ_0 can be deduced¹⁹ by taking $d(\text{JDOS})/d\hbar\nu = 0$ or $d\alpha/d\hbar\nu = 0$. According to Fig. 5(a), $d\alpha/d\hbar\nu$ vanishes at 0.340 eV, 0.354 eV, and 0.435 eV for GaAs, InGaAs, and GaAsSb,

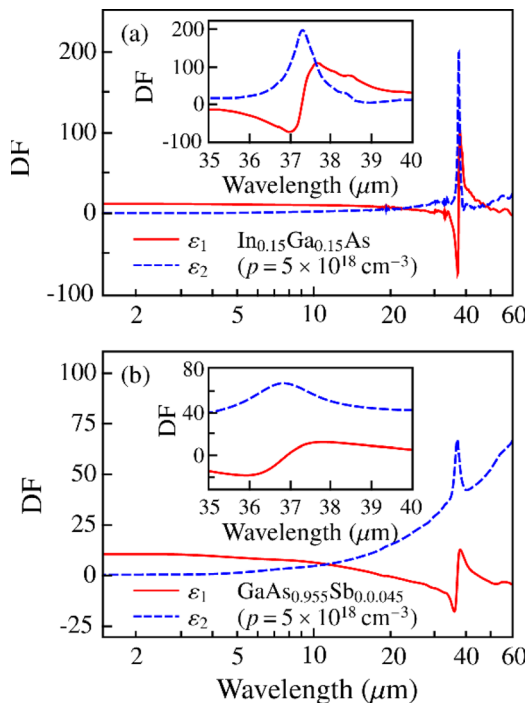


FIG. 5. Dielectric function (DF) of p -type (a) $\text{In}_{0.15}\text{Ga}_{0.85}\text{As}$ and (b) $\text{GaAs}_{0.955}\text{Sb}_{0.045}$ ($p = 5 \times 10^{18} \text{ cm}^{-3}$), with the insets showing the phonon region. The DF is obtained from the fittings as described in Sec. II.

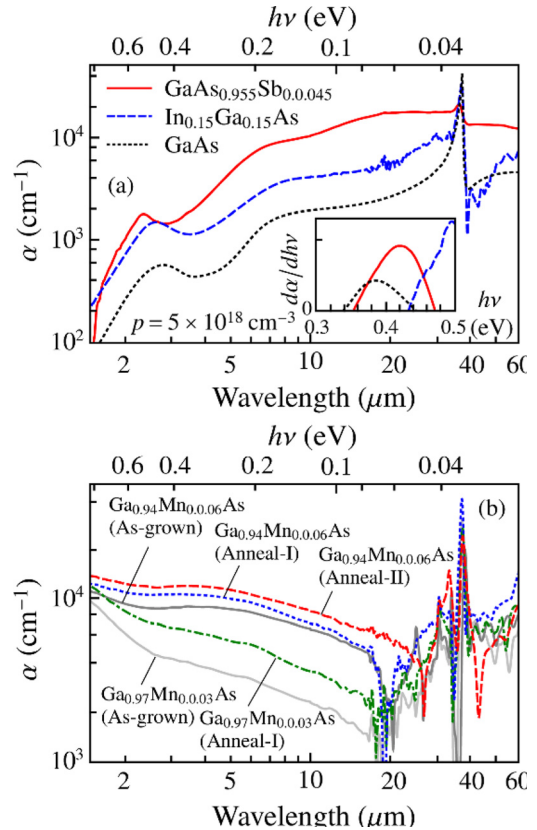


FIG. 6. Absorption coefficient (α) spectra extracted from the fitted DF, for p -type (a) $\text{In}_{0.15}\text{Ga}_{0.85}\text{As}$ and $\text{GaAs}_{0.955}\text{Sb}_{0.045}$, and (b) GaMnAs with different Mn fractions. There are fine features around 20 μm ($\text{In}_{0.15}\text{Ga}_{0.85}\text{As}$) in (a) and between 15 and 60 μm in (b) due to the experimental uncertainties. For annealing, the GaMnAs sample is cleaved into pieces, each of which was annealed with different durations at 230 $^{\circ}\text{C}$. Labels I and II correspond to a duration of 30 and 60 min, respectively. The inset of (a) plots $d\alpha/d\hbar\nu$, where $d\alpha/d\hbar\nu = 0$ determines the energy values that correlates with the split-off gap Δ_0 .

respectively; these values can be compared with those determined by IPE spectroscopy for GaAs (0.339 eV)¹⁹ and calculated using the Vegard's law²¹ for InGaAs and GaAsSb (0.347 eV and 0.358 eV, respectively). The relatively large divergence in the value of Δ_0 of GaAsSb could be due to the influence from the shifting of the SO-HH transition and the strong FC absorption (see Fig. 5(b)). Such an influence causing the blue-shifting of the energy at which $d\alpha/d\hbar\nu$ vanishes at higher doping concentration is observed in p -type GaAs as well (Fig. 2(d)). Overall, the absorption spectra of p -type InGaAs and GaAsSb resemble that of p -type GaAs;¹ the SO-HH absorption peak correlates to the value of Δ_0 .

In contrast to InGaAs and GaAsSb with non-magnetic p -type doping, the absorption of GaMnAs displays very different features, as shown in Fig. 6(b): the absence of the absorption dip (between 3 and 5 μm as shown in Fig. 6(a)) and the broad absorption between 1 and 20 μm with reduced absorption in longer wavelengths. Also, the absorption of GaMnAs is much greater than that of p -type InGaAs and GaAsSb, owing to its very high hole concentration.²⁴ Such a behavior of absorption could make GaMnAs be suitable for photodetectors to fully cover the 3–5 μm .

The intra-band FC absorption is typically proportional to λ^p ,^{28,29} where λ is the wavelength, and p is an exponent.

$p=2$ can be predicted by the Drude theory;²⁹ however, the deviation of p from 2 can be explained by the scattering mechanism;²⁹ for example, p equals 1.2, 2.5, and 3.5 corresponding to scatterings by acoustic phonons, polar optical phonons, and ionized impurities, respectively.²⁸ Nevertheless, the FC absorption, in general, increases with wavelength as being observed in p -type InGaAs and GaAsSb, as well as GaAs (Fig. 6(a)). As for GaMnAs, owing to its significantly high concentration of holes, the plasma frequency is greater than that of p -type doped InGaAs, GaAsSb, or GaAs. Therefore, the spectral range where the primary FC absorption takes place moves to the shorter wavelength region, i.e., towards the MWIR.

The behavior of Mn in GaMnAs has dual roles being either a donor or an acceptor. The interstitial Mn acts as a donor that compensates holes provided by substitutional MnGa. A post-growth annealing was thus carried out to reduce the interstitial Mn and increases the hole concentration.^{37,39,40} A constant annealing temperature at 230 °C with different annealing durations was carried out. The annealing temperature at which Mn interstitials can be efficiently reduced is experimentally determined to be around its growth temperature ranging from 180 °C to 250 °C.³⁷ Higher temperatures could result in the emergence of second phase, such as hexagonal NiAs-type MnAs, due to the metastability of GaMnAs. However, with a lower temperature, a much longer annealing time will be required. For these reasons, the annealing temperature was fixed at 230 °C.

Following the same fitting procedure, the absorption spectra of the annealed samples were obtained, as plotted in Fig. 6(b). It is apparent that the absorption increases with the annealing time, indicating increased hole concentration by the annealing process. The absorption spectra have a nearly parallel and upward shift by comparing with those of as-grown samples, owing to the increased hole concentration upon annealing. There is an absorption shoulder at about 5 μm which slightly shifts towards the short wavelength compared to the as-grown sample. The past reports (for example, by Jungwirth *et al.*⁴¹) have shown the blue-shifting of the MWIR absorption peak with increasing Mn fraction (hole concentration); this indicates that the optical characteristics of GaMnAs are similar to (non-magnetic) p -type GaAs. From this point of view, GaMnAs can be regarded as a p -type material with much high hole concentration.

Based on the obtained DF, optical conductivity can be readily calculated, with the real component shown in Fig. 7 for different samples. The relationship between the conductivity and hole concentration can be obtained through a sum rule

$$\frac{p}{m^*} = \frac{2}{\pi e^2} \int_0^{\Omega} \sigma_1(\omega) d\omega, \quad (13)$$

where p is the hole concentration, m^* is the effective mass, and Ω is a cutoff frequency. p/m^* denotes the spectral weight. The spectral profile of the conductivity is composed of contributions from individual transitions. The spectra of Ga_{0.97}Mn_{0.03}As are nearly featureless, while Ga_{0.94}Mn_{0.06}As has an absorption shoulder at $\sim 2000 \text{ cm}^{-1}$ that shifts to

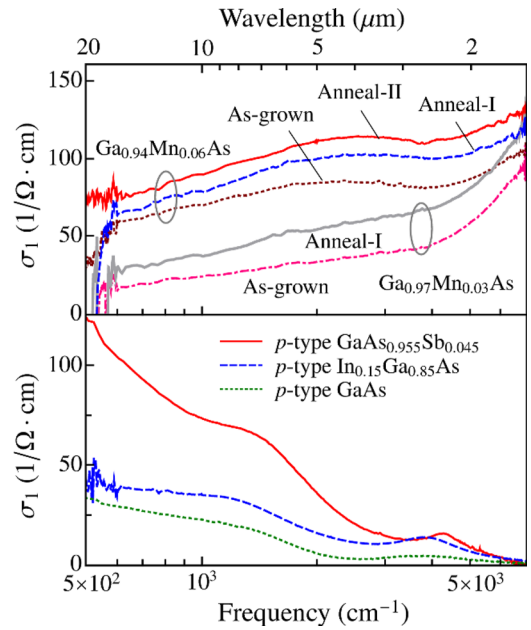


FIG. 7. The real component of conductivity (σ_1) for different samples. Labels I and II correspond to annealing (at 230 °C) with a duration of 30 and 60 min, respectively. The spectral profile of GaMnAs displays indistinct features by comparing with p -type InGaAs and GaAsSb. The strong intra-band free carrier absorption (in the low-frequency range) contributes to the far infrared conductivity significantly, whereas the IVB transitions have the dominant contribution in MWIR. The fine features below 600 cm^{-1} are due to experimental uncertainties.

higher frequency with increasing annealing time. For InGaAs and GaAsSb (Figs. 7(b) and 7(c)), strong intra-band FC absorption (in the low-frequency range) contributes to the far infrared conductivity significantly, whereas the IVB transitions have the dominant contribution in the MWIR infrared range. Fig. 8 shows the calculated spectral weights where p -type GaAs ($p = 8 \times 10^{18} \text{ cm}^{-3}$) is also shown for comparison. The spectral weight increases with increasing Mn fraction and annealing timing for GaMnAs due to the higher hole concentration.

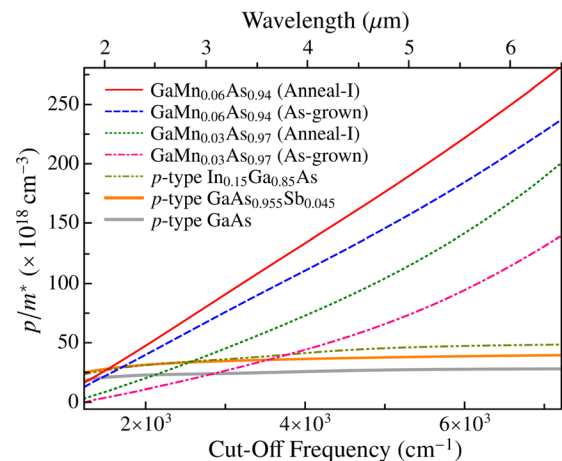


FIG. 8. The spectral weight calculated for different samples. The label I corresponds to annealing (at 230 °C) with a duration of 30 min. The p -type In_{0.15}Ga_{0.85}As and GaAs_{0.955}Sb_{0.045} are doped at $5 \times 10^{18} \text{ cm}^{-3}$, and p -type GaAs is with $8 \times 10^{18} \text{ cm}^{-3}$. The same fitting process as that applied to the samples in this study was used to obtain the DF and spectral weight of p -type GaAs.

The obtained absorption characteristics of GaMnAs imply its potential applications in developing IPE photodetectors operating based on holes. The 3–5 μm wavelength range of detection can be covered by using GaMnAs as the emitter to absorb photons effectively. This will be a great improvement over the p -type GaAs/AlGaAs heterojunction detectors which has a distinct response dip at around 3.6 μm .^{5,6}

V. SUMMARY

To summarize, the optical characteristics of p -type GaAs-based semiconductors including InGaAs, GaAsSb, and GaMnAs are reported. A comprehensive DF model independent of individual optical processes is used to extract the optical constants from experimental reflection and transmission spectra. In comparison with the previous model¹ based on analytic functions, this DF model produces optimum fitting results in the entire infrared region. The results indicate the correlation of the absorption due to the IVB transitions with the split-off gap (Δ_0). Different from the absorption of non-magnetic p -type doped InGaAs and GaAsSb that contains an absorption dip between 3 and 5 μm because of the forbidden SO-HH transition at the Γ point, GaMnAs displays a broad and enhanced absorption without degradation over 1–20 μm , due to its significantly high concentration of holes compared to regular p -type materials, such as InGaAs, GaAsSb, and GaAs. This characteristic of GaMnAs will make it a good candidate to develop IPE MWIR photodetectors.

ACKNOWLEDGMENTS

This work was supported, in part, by the U.S. Army Research Office under Grant No. W911NF-15-1-0018 monitored by Dr. William W. Clark, and, in part, by the U.S. National Science Foundation under Grant No. ECCS-1232184.

¹Y.-F. Lao and A. G. U. Perera, *J. Appl. Phys.* **109**, 103528 (2011).

²F. Shepherd, V. Vickers, and A. Yang, "Schottky barrier photodiode with a degenerate semiconductor active region," U.S. patent 3,603,847 (7 September 1971).

³T. L. Lin and J. Maserjian, *Appl. Phys. Lett.* **57**, 1422 (1990).

⁴A. G. U. Perera, H. X. Yuan, and M. H. Francombe, *J. Appl. Phys.* **77**, 915 (1995).

⁵P. V. V. Jayaweera, S. G. Matsik, A. G. U. Perera, H. C. Liu, M. Buchanan, and Z. R. Wasilewski, *Appl. Phys. Lett.* **93**, 021105 (2008).

⁶Y. F. Lao, P. K. D. D. P. Pitigala, A. G. U. Perera, H. C. Liu, M. Buchanan, Z. R. Wasilewski, K. K. Choi, and P. Wijewamasuriya, *Appl. Phys. Lett.* **97**, 091104 (2010).

⁷Y.-F. Lao and A. G. U. Perera, *Adv. Optoelectron.* **2016**, 1.

⁸B. F. Levine, S. D. Gunapala, J. M. Kuo, S. S. Pei, and S. Hui, *Appl. Phys. Lett.* **59**, 1864 (1991).

⁹S. D. Gunapala, B. F. Levine, D. Ritter, R. Hamm, and M. B. Panish, *J. Appl. Phys.* **71**, 2458 (1992).

¹⁰D. K. Sengupta, S. L. Jackson, D. Ahmari, H. C. Kuo, J. I. Malin, S. Thomas, M. Feng, G. E. Stillman, Y. C. Chang, L. Li, and H. C. Liu, *Appl. Phys. Lett.* **69**, 3209 (1996).

¹¹A. Shen, H. C. Liu, F. Szmulowicz, M. Buchanan, M. Gao, G. J. Brown, and J. Ehret, *J. Appl. Phys.* **86**, 5232 (1999).

¹²F. Szmulowicz, A. Shen, H. C. Liu, G. J. Brown, Z. R. Wasilewski, and M. Buchanan, *Phys. Rev. B* **61**, 13798 (2000).

¹³T. Elsaesser, M. Woerner, M. T. Portella, W. Frey, C. Ludwig, and A. Lohner, *Semicond. Sci. Technol.* **9**, 689 (1994).

¹⁴M. Woerner, T. Elsaesser, and W. Kaiser, *Phys. Rev. B* **45**, 8378 (1992).

¹⁵S. M. Sze and K. K. Ng, *Physics of Semiconductor Devices* (John Wiley & Sons, New York, 2007), Chap. 13.

¹⁶Y.-F. Lao, A. G. U. Perera, L. H. Li, S. P. Khanna, E. H. Linfield, and H. C. Liu, *Nat. Photonics* **8**, 412 (2014).

¹⁷Y.-F. Lao, A. G. U. Perera, L. H. Li, S. P. Khanna, E. H. Linfield, Y. H. Zhang, and T. M. Wang, *Opt. Lett.* **41**, 285 (2016).

¹⁸F. D. Shepherd and A. C. Yang, *Electron Devices Meeting, 1973 International*, 313 (1973).

¹⁹Y.-F. Lao, A. G. U. Perera, L. H. Li, S. P. Khanna, E. H. Linfield, and H. C. Liu, *Phys. Rev. B* **88**, 201302 (2013).

²⁰P. Lautenschlager, M. Garriga, S. Logothetidis, and M. Cardona, *Phys. Rev. B* **35**, 9174 (1987).

²¹I. Vurgaftman, J. R. Meyer, and L. R. Ram-Mohan, *J. Appl. Phys.* **89**, 5815 (2001).

²²H. Ohno, A. Shen, F. Matsukura, A. Oiwa, A. Endo, S. Katsumoto, and Y. Iye, *Appl. Phys. Lett.* **69**, 363 (1996).

²³A. Rogalski and M. Kimata, *Infrared Photon Detectors*, SPIE Press Monographs (Spie - Optical Engineering Press, 1995).

²⁴M. J. Seong, S. H. Chun, H. M. Cheong, N. Samarth, and A. Mascarenhas, *Phys. Rev. B* **66**, 033202 (2002).

²⁵R. Newman and W. W. Tyler, *Phys. Rev.* **105**, 885 (1957).

²⁶S. L. Chuang, *Physics of Optoelectronic Devices* (Wiley, New York, 1995).

²⁷S. Adachi, *Phys. Rev. B* **35**, 7454 (1987).

²⁸S. Adachi, *GaAs and Related Materials: Bulk Semiconducting and Superlattice Properties* (World Scientific, 1994), Chap. 11.

²⁹P. Y. Yu and M. Cardona, *Fundamentals of Semiconductors: Physics and Materials Properties* (Springer-Verlag Berlin, Heidelberg, 2005), Chap. 6.

³⁰A. G. U. Perera, H. X. Yuan, S. K. Gamage, W. Z. Shen, M. H. Francombe, H. C. Liu, M. Buchanan, and W. J. Schaff, *J. Appl. Phys.* **81**, 3316 (1997).

³¹A. L. Korotkov, A. G. U. Perera, W. Z. Shen, J. Herfort, K. H. Ploog, W. J. Schaff, and H. C. Liu, *J. Appl. Phys.* **89**, 3295 (2001).

³²M. B. M. Rinzan, D. G. Esae, A. G. U. Perera, S. G. Matsik, G. von Winkel, A. Stintz, and S. Krishna, *Appl. Phys. Lett.* **85**, 5236 (2004).

³³Z. G. Hu, M. B. M. Rinzan, S. G. Matsik, A. G. U. Perera, G. von Winkel, A. Stintz, and S. Krishna, *J. Appl. Phys.* **97**, 093529 (2005).

³⁴Z. G. Hu, M. Strassburg, N. Dietz, A. G. U. Perera, A. Asghar, and I. T. Ferguson, *Phys. Rev. B* **72**, 245326 (2005).

³⁵A. Afzali-Kushaa and G. I. Haddad, *J. Appl. Phys.* **77**, 6549 (1995).

³⁶A. B. Kuzmenko, *Rev. Sci. Instrum.* **76**, 083108 (2005).

³⁷K. W. Edmonds, P. Boguslawski, K. Y. Wang, R. P. Campion, S. N. Novikov, N. R. S. Farley, B. L. Gallagher, C. T. Foxon, M. Sawicki, T. Dietl, M. Buongiorno Nardelli, and J. Bernholc, *Phys. Rev. Lett.* **92**, 037201 (2004).

³⁸J. S. Blakemore, *J. Appl. Phys.* **53**, R123 (1982).

³⁹T. Hayashi, Y. Hashimoto, S. Katsumoto, and Y. Iye, *Appl. Phys. Lett.* **78**, 1691 (2001).

⁴⁰H. Riahi, W. Ouerghui, L. Thevenard, C. Gourdon, M. Maaref, A. Lematre, O. Manguin, and C. Testelin, *J. Magn. Magn. Mater.* **342**, 149 (2013).

⁴¹T. Jungwirth, P. Horodyská, N. Tesařová, P. Němec, J. Šubr, P. Malý, P. Kužel, C. Kadlec, J. Mašek, I. Němec, M. Orlita, V. Novák, K. Olejník, Z. Šobán, P. Vašek, P. Svoboda, and J. Sinova, *Phys. Rev. Lett.* **105**, 227201 (2010).